Exploring Low-Frequency ST-FMR: Simulation and Experiment

Logan Bishop-Van Horn*, Neal Reynolds, Samuel Brantley, Daniel C. Ralph†

Cornell Center for Materials Research REU

Summer 2016

Abstract

The field of spintronics, in which electrons are manipulated by way of their spin degree of freedom, shows great potential to form the basis for next generation data storage and computation technologies. Spin transfer torque-driven ferromagnetic resonance (ST-FMR) is a widely-used method for measuring current-generated spin transfer torques by exciting resonance precession in a thin magnetic film using microwave currents. In particular, ST-FMR is often used to determine the spin Hall angle, Θ_{SH}, the figure of merit for the spin Hall effect, a conversion of longitudinal charge current into transverse spin current via spin-orbit coupling. In this work we examine the accuracy of ST-FMR at low frequency as a function of sample dimensions, using both simulation and experiment.

I. Introduction

Spin transfer torques, in which a torque is applied to a nanoscale magnet by injection of a spin-polarized current, have been widely studied as alternatives to charge-based magnetic manipulation for data storage and computation applications [1,2]. The spin Hall effect, a conversion of charge current into transverse spin current via spin-orbit coupling, is one mechanism by which to generate spin currents to apply spin transfer torques [3,4]. The spin Hall angle, a figure of merit for the spin Hall effect, is defined as $\Theta_{\mathrm{SH}} \equiv J_s / J_c$, where J_s is the spin current density and J_c is the charge current density. In a normal metal/magnetic film multilayer, charge current flowing through a metallic layer with a large spin Hall angle will inject a spin current into the magnetic layer, applying a torque to the magnetization. Accurate measurement of the spin Hall angle is critical for the development of spin orbit torque-based technologies.

A common method for measuring the spin Hall angle in magnetic multilayers is spin transfer torque-driven ferromagnetic resonance (ST-FMR). In ST-FMR, resonant precession of the magnetic layer is excited by applying a microwave charge current. The magnetization experiences a torque due to the Oersted field from the radio frequency (rf) charge current and a spin transfer torque due to the injection of spin current from the metallic layer via the spin Hall effect. The theory behind ST-FMR relies upon the *macrospin approximation*, which assumes the magnetic layer acts as a single spin. The magnetization is modeled as a unit

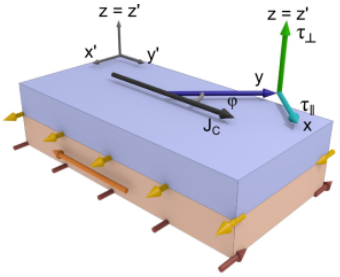

Figure 1: *Coordinate system used for micromagnetic model and ST-FMR analysis [5].*

*logan.bvh@gmail.com
†dcr14@cornell.edu

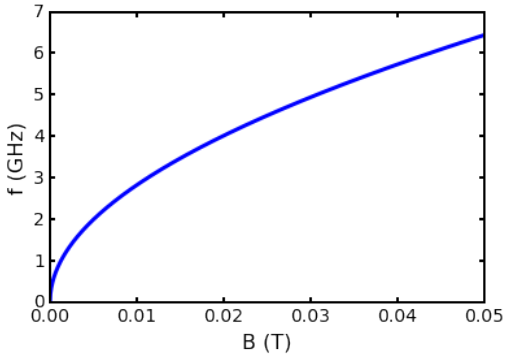

Figure 2: *Resonant frequency as a function of in-plane magnetic field for a film with $M = 8 \times 10^5$ A/m, from the Kittel formula.*

vector $\hat{m}(t) = m_x(t)\hat{x} + \hat{y} + m_z(t)\hat{z}$, which lies almost entirely in the y direction, with small arbitrary x and z components (see Figure 1).

The time evolution of the magnetization is described by the Landau-Lifshitz-Gilbert-Slonczewski (LLGS) equation [1]:

$$\dot{\hat{m}} = \underbrace{-\gamma\, \hat{m} \times \vec{H}_{\text{eff}}}_{\text{(demagnetization)}} + \underbrace{\alpha\, \hat{m} \times \dot{\hat{m}}}_{\text{(Gilbert damping)}} + \underbrace{\frac{\gamma\hbar \cos\varphi}{2e\mu_0 M_s} J_s\, \hat{m} \times (\hat{\sigma} \times \hat{m})}_{\text{(spin transfer torque)}} - \underbrace{\gamma \cos\varphi\, \hat{m} \times \vec{H}_{\text{Oe}}}_{\text{(Oersted torque)}}$$

Here, $\dot{\hat{m}}$ denotes the time derivative of the magnetization unit vector, γ is the gyromagnetic ratio, $\vec{H}_{\text{eff}}$ is the effective external field, α is the Gilbert damping coefficient, μ_0 is the permeability of free space, $\hbar$ is the reduced Planck constant, φ is the angle between the charge current and the external magnetic field, M_s is the saturation magnetization of the magnetic layer, J_s is the spin current density, $\hat{\sigma}$ is the direction of spin polarization, and $\vec{H}_{\text{Oe}}$ is the Oersted field. The resonance condition for a thin film with with in-plane external field is given by the Kittel formula: $f = \frac{\gamma}{2\pi}\sqrt{B(B + \mu_0 M)}$ [6]. Here, f is the resonant frequency, B is the external field strength, and M is the film's magnetization. The resonant precession of the magnetization leads to rf oscillations in the magnetic layer resistivity due to anisotropic magnetoresistance (AMR, the dependence of resistance on the angle between the magnetization and the current). These rf oscillations in resistance mix with the rf charge current to produce a dc resonance curve. Analytical solutions to the LLGS equation predict a resonance curve that is the sum of a symmetric Lorentzian and an anti-symmetric Lorentzian, due to the spin transfer and Oersted torques, respectively (see Figure 3). The spin Hall angle can be extracted from fits to the ST-FMR resonance curves [3].

Figure 3: *Components of the ST-FMR curve.*

Low-frequency (i.e. $<$ 5GHz) ST-FMR has not been thoroughly studied. It is not known to what extent the macrospin approximation holds in this frequency regime, where the resonant field may not be strong enough to fully saturate the magnetic layer (see Figure 2). It is also not known what role spatial variations in the magnetization dynamics play in the final determination of Θ_{SH}. To begin to answer these questions, we examine low-frequency ST-FMR in magnetic bilayers as a function of sample dimensions using a combination of experiment and simulation.

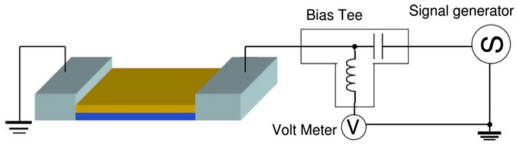

Figure 4: *Schematic of ST-FMR measurement set-up [3].*

II. Methods

i. Experiment

i.1 Experimental Setup

We performed ST-FMR measurements on thin film bilayers of the form [sapphire substrate/normal metal layer (thickness in *nm*)/magnetic layer (thickness in *nm*)/thin capping layer to protect device]. Data presented below are from Pt (6)/Py (5.4) and Pt (6)/Py (10.8) (Py=Permalloy≡$Ni_{81}Fe_{19}$) samples with an Hf capping layer to prevent oxidation, and Pt (6)/CoFeB (6)/Al capping layer samples. The films were grown using dc magnetron sputter deposition in CCMR, and fabricated at CNF into devices with dimensions from 2 to 100 microns with varying aspect ratio. Ground-signal-ground waveguides were added to each device to create rf contact.

The ST-FMR measurement is performed as follows:

- Measure AMR of device using rotating projected-field magnet
- Measure the rf transmission and reflection characteristics of the device and auxilliary cabling
- Field sweep:
  - Apply charge current at fixed frequency and power
  - Set $\varphi = 45$ degrees between the external field and charge current
  - Sweep external field
  - Measure dc mixing voltage
  - Step frequency, and repeat

The rf charge current is supplied by a signal generator through a bias tee (see Figure 4). The Oersted field and spin Hall effect-generated transverse spin current apply torques to the magnetization, resulting in small-angle precession. This causes oscillations in the resistance of the device due to AMR. These rf resistance oscillations mix with the rf charge current, resulting in a dc signal that is measured at the dc port of the bias tee. In order to maximize signal-to-noise, we perform amplitude modulation of the supplied current at $\sim$ 1kHz and use a lock-in amplifier locked in to this low-frequency signal to measure the dc mixing voltage.

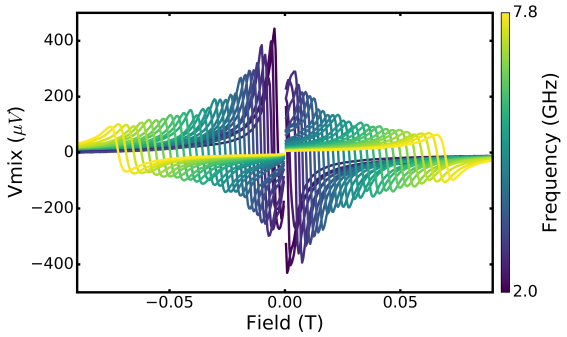

Figure 5: *Experimental ST-FMR data for a* $20\mu m \times 4\mu m$ *Pt (6)/Py (10.8) device.*

i.2 Analysis

Figure 5 shows a typical sequence of ST-FMR curves at frequencies from 2-7.8GHz. In order to extract Θ_{SH} from this data, the following analysis must be performed:

- Calculate how much current is flowing through the device using the measured rf characteristics of the experimental setup
- Calculate how much current is flowing through the normal metal layer of the device using the resistivity of the normal metal material and the total device resistance (parallel resistor model)
- Fit the data to a sum of symmetric and anti-symmetric Lorentzians to extract the following fit parameters:
  - C_x: Symmetric component amplitude
  - C_z: Anti-symmetric component amplitude
  - α: Gilbert damping coefficient
  - M_{eff}: effective magnetization

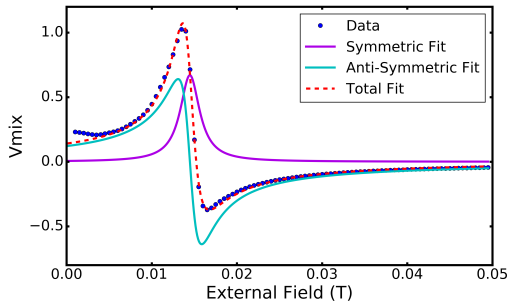

Figure 6: *Typical positive field ST-FMR curve and fit.*

- Multiply the ratio C_x/C_z by M_{eff} and set of constants based on the sample dimensions and experimental parameters to obtain Θ_{SH}, the "S over A" spin Hall angle

Using this fitting routine, we can examine the determined value of the spin Hall angle, effective magnetization, and Gilbert damping as a function of sample dimensions and frequency. Figure 6 shows a typical ST-FMR curve with symmetric and anti-symmetric fits.

ii. Micromagnetic Simulation

Computer simulations allow us to explore the magnetization dynamics of thin films on submicron length scales, allowing us to investigate the validity of the macrospin approximation in ST-FMR for various sample dimensions, materials, and frequencies. In contrast with macrospin analysis, in which it is assumed that the magnetization of the entire layer can be described by a single vector, micromagnetic analysis breaks up a sample into many cells or *microspins* and calculates their interaction amongst themselves and with the external excitations (e.g. field and spin current). We use MuMax3 GPU-accelerated micromagentic software in the cloud utilizing AWS Elastic Cloud Compute [7,8]. Using MuMax3 we can calculate the instantaneous spatial distribution of the magnetization for visualization or animation. We can also output the vector components of the unit magnetization as a function of time, averaged over all or part of the magnetic layer.

The micromagnetic model for ST-FMR has the following components (see Figure 1 for coordinate system):

- In-plane magnetized (y direction) magnetic layer with set dimensions and material parameters:
  - Saturation magnetization
  - Gilbert damping
  - Exchange strength
- rf charge current in y' direction and resulting Oersted field
- In-plane external field at an angle φ relative to the rf charge current
- Spin current in $z = z'$ direction, with polarization in x' direction and spin current density J_s determined by fixed spin Hall angle $\Theta_{\text{SH}} \equiv J_s/J_c$

ii.1 Simulated ST-FMR

In order to evaluate the extent to which micromagnetic simulations can simulate ST-FMR, we turn first to the task of simulating the dc mixing voltage which comprises our experimental data. Since experimental ST-FMR results arise from the AMR of the entire sample, we need to examine the x' component of the magnetization averaged over the whole film. In MuMax3 we perform field sweeps at a sequence of frequencies, just as in ST-FMR experiments. The output from these simulations is a single text file containing the vector components of the spatially-averaged magnetization as a function of time for all field sweeps performed (see Figure 7). MuMax3 uses an adaptive time step ODE solver, resulting in arbitrary time spacing. The first step in data processing is to perform a cubic spline to obtain data that is evenly spaced in time. To obtain ST-FMR data from these simulations the following steps are performed:

- For each frequency:
  - For each field:
    - Identify the time period corresponding to this field
    - Disregard the first half of this time period (transient)
    - Multiply the $m_{x'}$ signal from the second half of this time period

by $\sin(2\pi \cdot f \cdot t)$, where f is the frequency of the rf current and t is time

* Integrate the multiplied signal over $n \in \mathbb{N}$ periods and divide by $T = n/f$ to simulate the mixing of the rf resistance and rf current

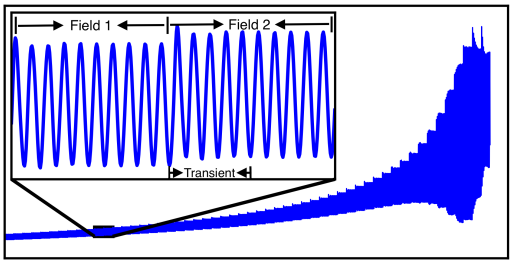

Figure 7: *x' component of the magnetization for a single MuMax3 field sweep The timescale of the inset (showing two field steps) is 10ns. Resonance is visible to the right of the inset. The first half of each field step is ignored to allow any transient to subside.*

This computation preserves both the amplitude and phase of the magnetization dynamics, resulting in ST-FMR curves as show in Figure 8. Once the ST-FMR curves are obtained, we can fit them to the Lorentzian model predicted by the LLGS equation (see Figure 6) to extract the parameters C_x (the symmetric Lorentzian amplitude), C_z (the anti-symmetric Lorentzian amplitude), M_{eff} (the effective magnetization in tesla), and α (the Gilbert damping coefficient). The "S over A" spin Hall angle is then given by

$$\Theta_{\text{SH}} = -\frac{C_x}{C_z}\frac{e}{\hbar}M_{\text{eff}}t^2$$

Here, e is the elementary charge and t is the thickness of the magnetic layer in meters.

III. Results

i. Experimental Results

Most of the experimental data obtained was from the Pt (6)/CoFeB (6) devices. Due to time constraints, a very limited amount of Pt/Py data was taken.

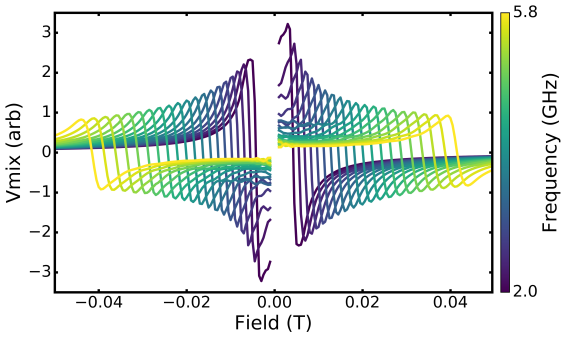

Figure 8: *Simulated ST-FMR data for a $20\mu m \times 4\mu m \times 10nm$ Py film with spin current corresponding to Θ_{SH} of Pt.*

i.1 CoFeB ST-FMR

Below is data demonstrating the low-frequency trends in Θ_{SH} as a function of sample dimensions. Except for extreme cases (i.e. frequencies below $\sim$ 4GHz, very high or very low aspect ratios), Θ_{SH} showed very good agreement with the expected value: $\approx$0.07 for Pt [9]. As can be seen in Figure 9, the determined value for Θ_{SH} begins to diverge with decreasing frequency below about 4GHz, at a rate that depends upon the sample length. A similar effect can be seen as a function of sample width where, all else equal, Θ_{SH} for narrower samples diverges faster than Θ_{SH} for wider samples. While the devices presented in the lower graph of Figure 9 are not all the same length, they are all long enough to be in a regime where relatively small differences in length do not cause significant changes in the trend in Θ_{SH}.

The dependence on sample dimensions is much greater at low frequencies than at higher frequencies. Figure 10 shows Θ_{SH} as a function of sample length and frequency for samples of two different widths. Particularly interesting is the $2\mu m$ wide sample, which shows a maximum in Θ_{SH} as a function of length that develops with decreasing frequency. Such a feature is not seen in wider samples. Graphs such as Figure 10 could serve as a useful roadmap for

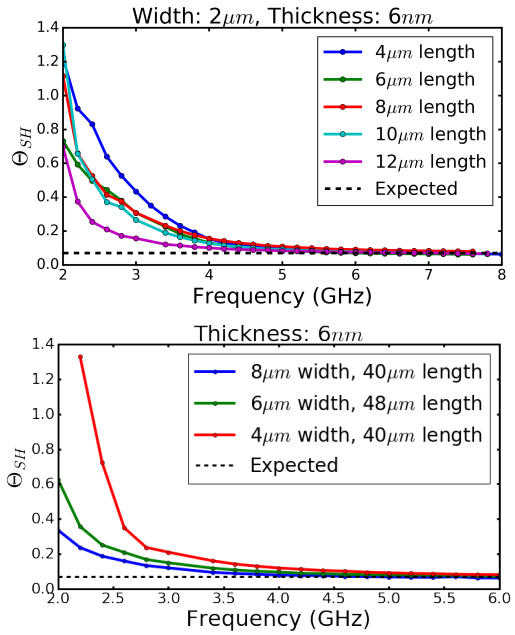

Figure 9: Θ_{SH} *for Pt (6)/CoFeB (6) samples with* 2μm *width and varying length (top) and varying width (bottom). The devices in the bottom graph are long enough that the small difference in length between them does not affect* Θ_{SH}*. The determined value for the spin Hall angle diverges at low frequencies, at a rate that depends on sample dimensions.*

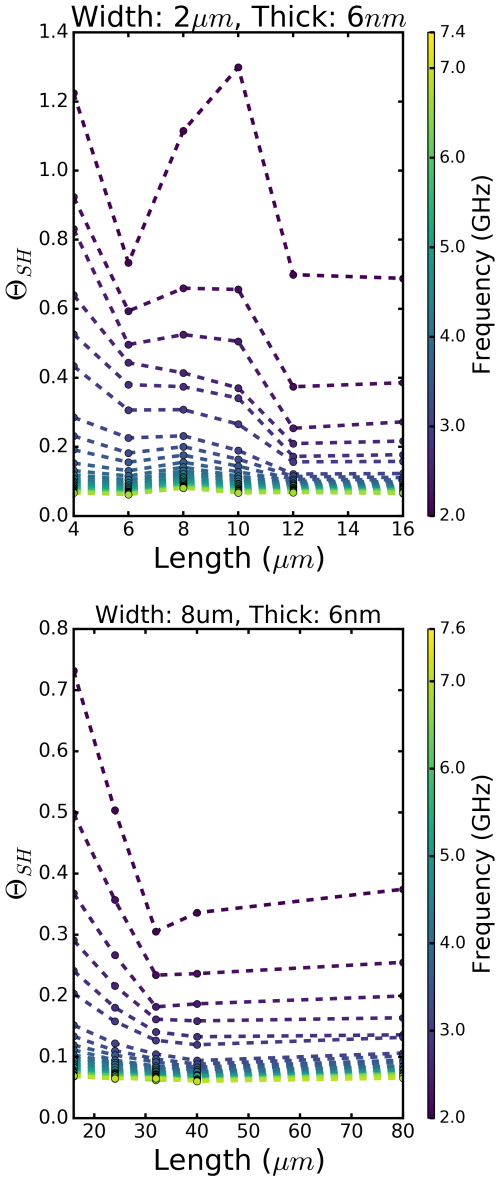

Figure 10: Θ_{SH} *as a function of sample length and frequency for two Pt (6)/CoFeB (6) samples of different widths.*

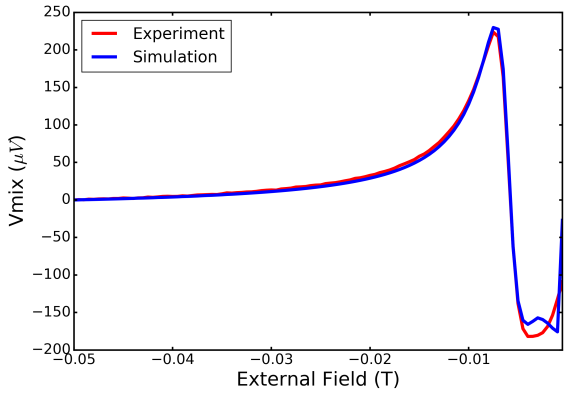

Figure 11: *Experimental and simulated ST-FMR curves for a $24\mu m \times 4\mu m \times 5.4nm$ Py layer at 2GHz. Simulation data has been scaled vertically by a constant factor.*

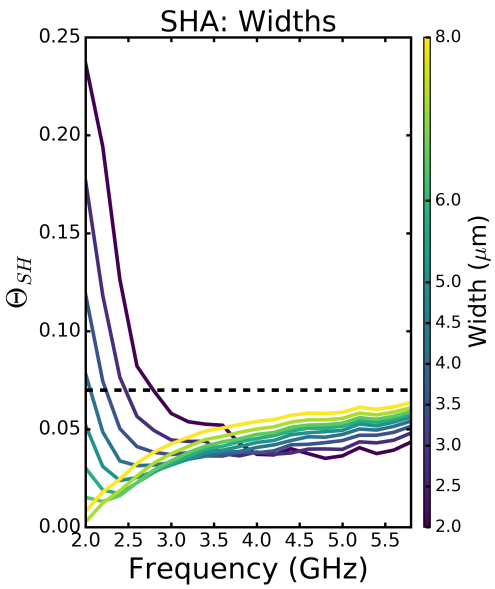

Figure 12: *Simulated Θ_{SH} for $20\mu m$ long, $6nm$ thick Py samples as a function of frequency and sample width. The dotted black line shows the actual spin Hall angle*

determining over which regions of parameter space ST-FMR results are valid.

ii. Simulation Results

To evaluate the validity of the micromagnetic model, the effective magnetization M_{eff} and Gilbert damping coefficient α were extracted from fits to the Lorentzian model for experimental ST-FMR data from a $24\mu m \times 4\mu m$ Pt (6)/Py (5.4) device. These parameters were then used to model a device with the same dimensions. Figure 11 shows both experimental and simulated ST-FMR curves for a field sweep at 2GHz. The simulated data (whose amplitude is arbitrary) has been scaled vertically by a constant factor. Clearly there is very good agreement between simulation and experiment, even in a frequency regime where the macrospin approximation may not hold.

One difficulty with this type of analysis is that M_{eff} and α are not well constrained under the current fitting method, so their values tend to drift as a function of frequency (see Figure 17). The micromagnetic model uses a single value for these parameters for all frequencies. The result is that the experimental and simulated ST-FMR curves do not agree to the same extent across a whole frequency sweep.

ii.1 Θ_{SH} Measurements

We examined Θ_{SH} extracted from micromagnetic simulation data using the "S over A" method described above. All of the simulations were of Permalloy samples, which makes it difficult to make quantitative comparisons to the CoFeB experimental results. Qualitatively, however, the simulations reproduce the trends in Θ_{SH} at low frequency. Figure 12 shows the simulated ST-FMR-determined spin Hall angle $20\mu m$ long, $6nm$ thick Py samples as a function of frequency and sample width. The divergence in Θ_{SH} with decreasing frequency for narrower samples is consistent with the results from CoFeB measurements. For wider samples, however, the simulated spin Hall angle decreases with decreasing frequency, which we do not see experimentally. Figure 13 shows that for thicker samples, the ST-FMR-determined value for Θ_{SH} in thicker magnetic films is suppressed for "intermediate" frequencies ($\sim$ 3 GHz$-$ $\sim$ 6 GHz). We do not have experimental data, either CoFeB or Permalloy, to which to compare this result.

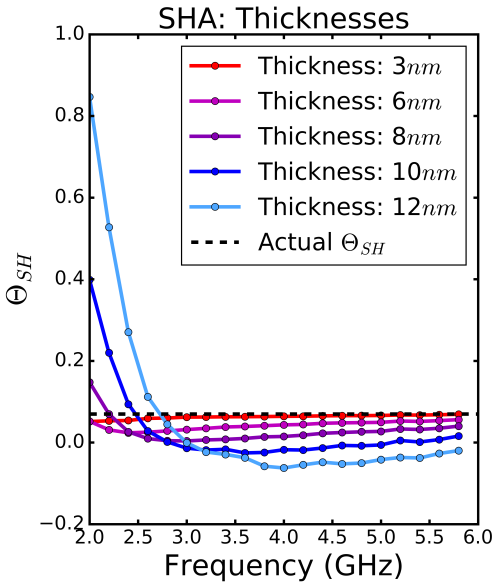

Figure 13: *Simulated ST-FMR-determined Θ_{SH} as a function of frequency and magnetic layer thickness for a $20\mu m \times 4\mu m$ Py samples. The dotted black line shows the actual spin Hall angle.*

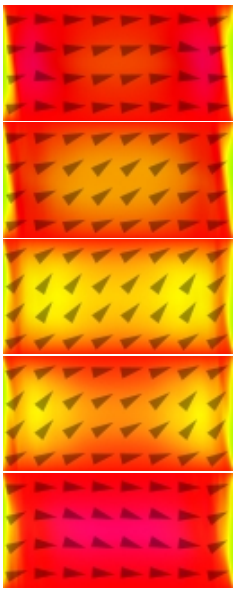

Figure 14: *Visualization of the magnetization of a $10\mu m \times 1\mu m \times 6nm$ Py film, driven at 2.4GHz, over roughly one period near resonance. The triangles and color represent the direction of the magnetization in different regions*

ii.2 Spatial Analysis

Given the form of the Kittel resonance condition (Figure 2), it is possible that at lower frequencies the resonant field is not strong enough satisfy the macrospin approximation. It is therefore desirable to examine the spatial variation in magnetization dynamics, which ST-FMR is not sensitive to. MuMax3 has the option to output spatial magnetization data either in the form of .jpg images (Figure 14) or .ovf files, which can be converted into images using other software.

As images like those in Figure 14 show, there are significant variations in the magnetization dynamics across the sample. In order to better understand these spatial variation, we examined the relative phase and amplitude of the magnetization precession in various regions of the sample.

Figure 15 shows that in a thin sample (6nm), the oscillations at the edge of the sample almost always lag the oscillations at the center. This is not surprising, as the material at the edge of the sample is more strongly influenced by the demagnetization field. The phase shift between the edge and center at resonance grows with decreasing frequency, which is not surprising as the resonant field is lower at lower frequencies.

In the thicker sample (12nm), the phase shift at resonance is larger for all frequencies, the region of large phase shift around resonance is wider, and the frequency of maximum phase shift is higher than in the 6nm sample. At higher frequencies, in addition to the minimum at resonance, we see maxima and minima in the phase difference as a function field below the resonant field. This is a very interesting result, and certainly warrants further investigation, both in experiment and in simulation.

We can also examine the amplitude of the magnetization precession in different regions of the sample. Figure 16 shows the precession amplitude in the edge and center regions of a $20\mu m \times 4\mu m \times 12nm$ Py film, as defined in the top image of Figure 15. The bottom

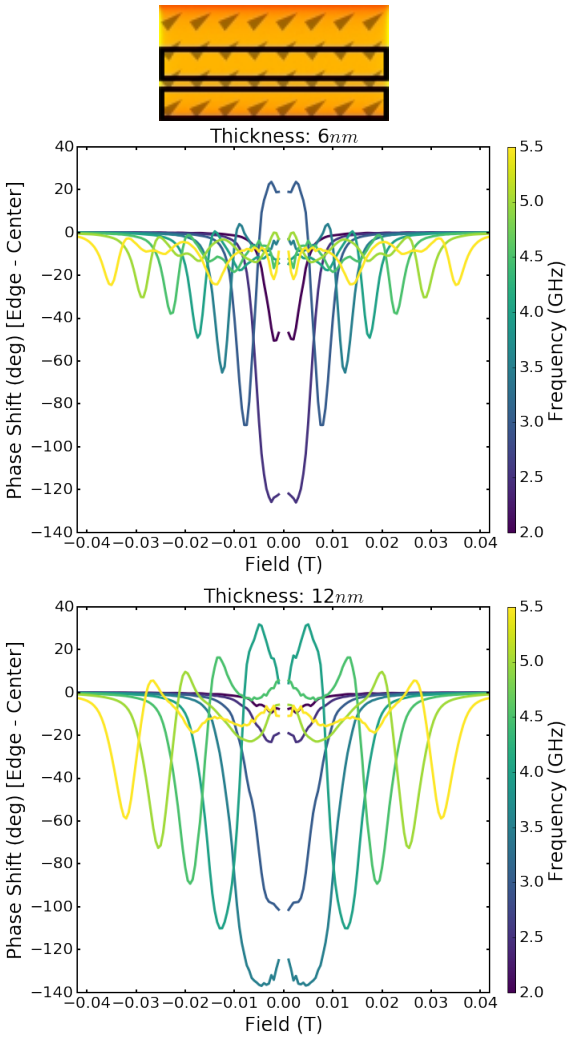

Figure 15: *Top: Center and edge regions. Long axis is the y' axis, short axis is the x' axis. Center and bottom: Phase shift between the center and edge of a $20\mu m \times 4\mu m$ simulated Py sample as a function of field for 6nm (center) and 12nm (bottom) films. Negative phase shift means the center "leads" the edge.*

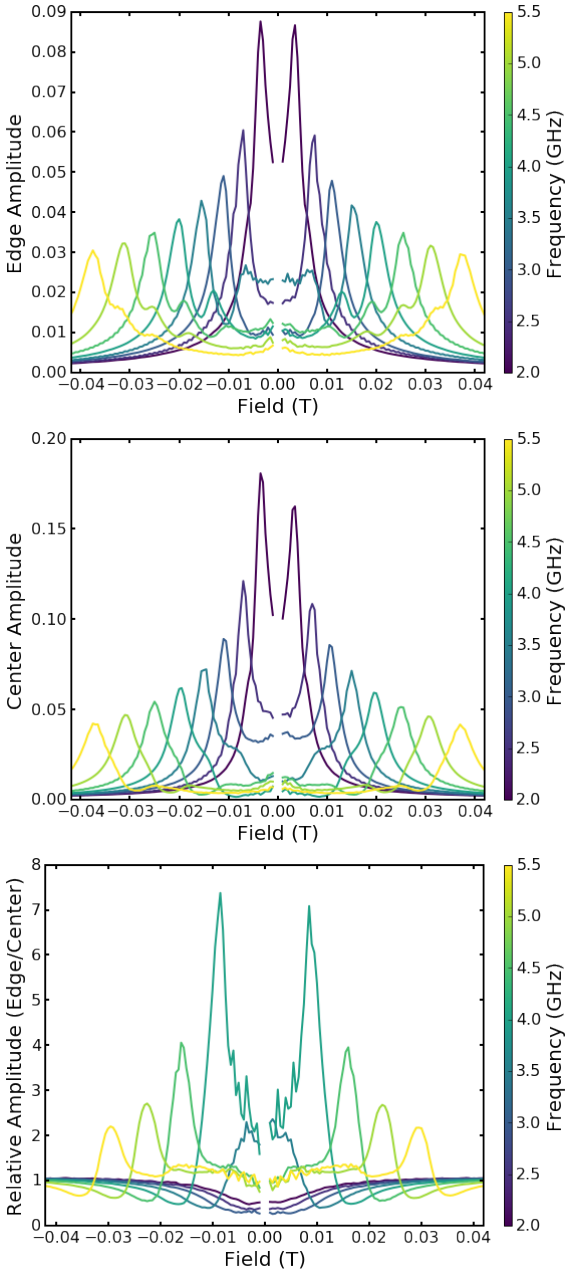

Figure 16: *Top and center: Precession amplitude at the edge and center of a $20\mu m \times 4\mu m \times 12nm$ Py film as a function of field. Bottom: relative precession amplitude (edge/center) between the two regions.*

panel shows the relative amplitude (edge amplitude/center amplitude) between the two regions. As expected, there is a maximum in both edge and center amplitudes at resonance. There is also a minimum in relative amplitude at resonance (meaning that the amount by which the center amplitude is larger is at a maximum). This is also to be expected. What is somewhat surprising is the maximum in relative amplitude after resonance (as the magnitude of the field decreases), for instance at about ± 0.015T in the 4.5GHz curve. It appears this is due to additional local maxima that develop in the edge amplitude (top graph) below the resonant field.

IV. Discussion

i. Lorentzian Model

As can be seen in Figure 11, given the right material parameters (saturation magnetization, Gilbert damping, and exchange strength), the micromagnetic model can very accurately recreate experimental ST-FMR curves. The effective magnetization, M_{eff}, and Gilbert damping coefficient, α, can be extracted from fits to experimental data. However, since these two parameters are strongly coupled and not well constrained, their values as determined by fitting to the Lorentzian model are not constant as a function of frequency (see Figure 17). In the future, even at high frequencies, it would likely be wise to fit both the experimental and simulated ST-FMR data to the more general Lorentzian form as described in Ref. [3].

It appears the ST-FMR curves are not a simple sum of Lorentzians at very low frequencies due to breakdown of the macrospin approximation, and therefore the extracted values for M_{eff} and α are not reliable in this regime. **It seems likely that the low frequency divergence in the determined value of the effective magnetization is main cause of the low frequency divergence in Θ_{SH}.** In both simulation and experiment, the nature of the divergence in M_{eff} seems to depend upon sample dimensions. This suggests the dimensions of the sample affect the way in which the magnetization dynamics differ from the macrospin model.

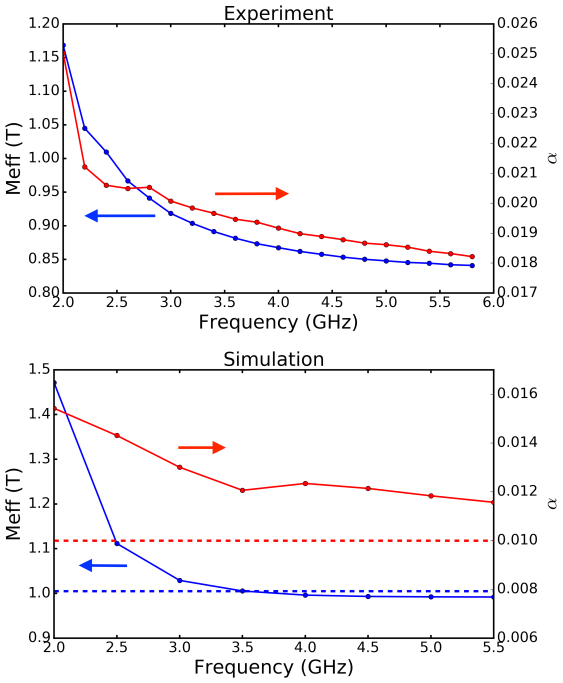

Figure 17: *Values for M_{eff} (blue) and Gilbert damping coefficient, α, (red) extracted from fits to experimental (top) and simulated (bottom) ST-FMR data. Experimental data is from a $24\mu m \times 4\mu m$ Pt (6)/Py(5.8) device. Dotted lines in simulated data show actual values for M_{eff} and α.*

ii. Sample Dimensions

It is clear from both the experimental CoFeB data and the simulated Py data that all three sample dimensions, length, width, and thickness, play an important role in the magnetization dynamics and ST-FMR measurements of thin films at low frequency. The experimental CoFeB data (Figures 9 & 10) shows dependence of the ST-FMR-determined spin Hall angle on sample length and width, and the simulated Py data (Figure 12) shows a similar dependence on sample width. Unfortunately we do not at this time have simulated CoFeB data to compare to experiment, nor do

we have enough experimental Py data to make detailed comparisons to simulation.

Figure 13 shows that the ST-FMR-determined value for Θ_{SH} in thick samples is suppressed at intermediate frequencies (roughly 3GHz−6GHz) and diverges at lower frequencies. **The suppression of Θ_{SH} in thick samples appears to be a result of destructive interference between different regions of the sample (see Figure 15).** However, this does not explain why the determined value of Θ_{SH} rises *above* the actual value at the lowest frequencies. **The most likely explanation for this is the divergence in the fit-determined value of M_{eff}, because in the ST-FMR analysis $\Theta_{SH} \propto M_{eff}$.** This is supported by the data in Figure 12, which appears to show two competing terms affecting Θ_{SH}: one term (the destructive interference between different regions) that tends to decrease Θ_{SH} with decreasing frequency, and another term (the divergence in M_{eff}) that tends to increase Θ_{SH} with decreasing frequency.

iii. Simulation Tools

We have developed a large set of tools for performing micromagnetic simulations of ST-FMR and analyzing and visualizing the results. These tools, written in Python, include:

- Standard ST-FMR analysis, including the calculation of Θ_{SH}
- Analysis and comparison of the phase and amplitude of 2-5 regions in a single sample
- Analysis and comparison of the phase and amplitude of up to 5 regions in two different samples (if, for example, one wants to change a material parameter and examine the effect that has on the spatial variation)
- Analysis of phase relative to driving current in two regions of a sample
- Tools for creating clear visualizations of the results of the above analyses

Micromagnetic ST-FMR simulations can serve as a very valuable probe into the microscopic phenomena that lead to the macroscopic data (i.e., the dc mixing signal). These simulations may also serve as a useful bridge to connect ST-FMR, which is not sensitive to spatial information about the magnetization dynamics, to other spatially-resolved measurements such as time-resolved anomalous Nernst effect (TRANE) microscopy [10] and Brillouin light scattering (BLS) spectroscopy [11], allowing clearer interpretation of results across measurement methods.

Acknowledgements: I would like to thank Neal Reynolds for his guidance this summer, Samuel Brantley for performing the device fabrication at CNF, and Dr. Ralph for his guidance and support. This work was made possible by the Cornell Center for Material Research, the Cornell NanoScale Science & Technology Facility, the NSF Research Experience for Undergraduates program (DMR-1460428 and DMR-1120296).

References

[1] Slonczewski, Current-driven excitation of magnetic multilayers. *J. Magn. Magn. Mater.*, **159**, L1-L7 (1996).

[2] Kiselev, *et al.*, Microwave oscillations of a nanomagnet driven by a spin-polarized current. *Nature*, **425**, (2003).

[3] Liu, *et al.*, Spin-Torque Ferromagnetic Resonance Induced by the Spin Hall Effect. *Phys. Rev. Lett.*, **106**, 036601 (2011).

[4] Liu, *et al.*, Spin-Torque Switching with the Giant Spin Hall Effect of Tantalum. *Science*, **336**, (2012).

[5] Mellnik, Notes on ST-FMR, http://alex.mellnik.net/notes-on-st-fmr/

[6] Kittel, Introduction to Solid State Physics 7th edn, 505 (John Wiley & Sons, New York, 1996).

[7] Vansteenkiste, *et al.*, The design and verification of MuMax3, *AIP Advances*, **4**, 107133 (2014).

[8] Jermain, *et al.* GPU-accelerated micromagnetic simulations using cloud computing. *J. Magn. Magn. Mater.*, **401**, 320-322 (2016).

[9] Liu, *et al.* Review and Analysis of Measurements of the Spin Hall Effect in Platinum. arXiv:1111.3702, (2012)

[10] Guo, *et al.* Ferromagnetic resonance phase imaging in spin Hall multilayers. *Phys. Rev. B*, **93**, 144415 (2016).

[11] Jungfleisch, *et al.* Large Spin-Wave Bullet in a Ferrimagnetic Insulator Driven by the Spin Hall Effect. *Phys. Rev. Lett.*, **116**, 057601 (2016).